Determination of the adsorption geometry of PTCDA on the Cu(100) surface

Simon Weiß,[1,2,*] Ina Krieger,[3] Timo Heepenstrick,[3] Serguei Soubatch,[1,2]
Moritz Sokolowski,[3] and F. Stefan Tautz[1,2]

[1]*Peter Grünberg Institut (PGI-3), Forschungszentrum Jülich, 52425 Jülich, Germany*
[2]*Jülich Aachen Research Alliance (JARA), Fundamentals of Future Information Technology, 52425 Jülich, Germany*
[3]*Institut für Physikalische und Theoretische Chemie der Universität Bonn, Wegelerstraße 12, 53115 Bonn, Germany*

(Received 3 May 2017; published 10 August 2017)

The adsorption geometry, namely the height and the site, of 3,4,9,10-perylene tetracarboxylic dianhydride (PTCDA) on the Cu(100) surface was determined by the normal incidence x-ray standing wave (NIXSW) technique including triangulation. The two PTCDA molecules in the superstructure unit cell, which have perpendicular azimuthal orientation, are both located at bridge sites, the long molecular axis being parallel to the bridge. Carboxylic oxygen atoms and several atoms of the carbon backbone are located close to on-top positions. The vertical distortion motif of PTCDA on Cu(100) differs from that on the three low-index Ag surfaces, because significant downward displacement of the carboxylic oxygen atoms is lacking. In particular, the carbon backbone of PTCDA adsorbs closer to the surface than extrapolated from Ag data. This suggests a relative increase of the attractive interactions between the carbon backbone of PTCDA and the Cu(100) surface versus the attractive interactions on the carboxylic oxygen atoms.

DOI: 10.1103/PhysRevB.96.075414

I. INTRODUCTION

The bonding between extended aromatic molecules and metal surfaces is complex, because several different interactions such as local covalent bonding, the more delocalized bonding between the extended π system and the surface, and van der Waals forces can be involved [1]. Moreover, the correct description of the bonding by theory is still a challenge, because the inclusion of long-range correlation effects, such as the van der Waals attraction, into density functional theory (DFT) is difficult, and also because the self-interaction error of DFT is particular severe for molecular systems [2]. Therefore it is essential to gain a precise knowledge of the key experimental observable, i.e., the geometric structure of the molecule-metal interface including both the lateral arrangement of the molecules and the intramolecular distortion, because the various interactions manifest themselves in the geometric structure.

PTCDA adsorbed on metal single crystals is one of the best investigated model systems in this context [3]. In particular, the geometric structures of PTCDA on Au(111) [4], Ag(111) [5–9], Ag(100) [10,11], Ag(110) [10,12], Cu(111) [8], and also on the $Cu_3Au(111)$ alloy surface [13] have been studied. Remarkably, these experiments have revealed a correlation of the van der Waals-corrected molecular adsorption heights with the work functions of the bare metal surface [9,14]. The van der Waals-corrected adsorption height h^{vdW} is defined as the difference of adsorption height h of the molecule with respect to the surface lattice planes and the van der Waals (vdW) radius $r^{\mathrm{vdW}}_{\mathrm{surface}}$ of the respective surface atom:

$$h^{\mathrm{vdW}} = h - r^{\mathrm{vdW}}_{\mathrm{surface}}. \quad (1)$$

This correlation can be rationalized by the charge spill out from the surface into the vacuum, which increases with the work function and which keeps the molecule away from the surface by Pauli repulsion [14]. It is accompanied by an increased charge transfer into the lowest unoccupied molecular orbital (LUMO) that is facilitated on lower work function surfaces [10].

A further tendency that has been observed in the studies of PTCDA on Ag surfaces is the downward bending of the carboxylic oxygen atoms towards the surface [5,8–10,12]. This bending has been explained by the formation of local covalent bonds between the carboxylic oxygen atoms and the nearest surface metal atoms [10]. Indeed, the carboxylic oxygen atoms tend to adsorb near on-top positions and pull the metal atoms to which they bind slightly out of the metal surface [10]. It has also been pointed out that the local oxygen-metal bonds and the more extended interactions between the π system and the metal reinforce each other [15].

Most remarkably, while PTCDA on Cu(111) follows the overall tendency of an increasing van der Waals corrected adsorption height with work function [9,14], it exhibits a different distortion motif: the carboxylic oxygen atoms move upwards to a level above that of the carbon backbone of the molecule [8]. This is in contrast to the situation on the Ag surfaces and points towards an entirely different interplay between local and extended bonds on Ag surfaces and Cu(111). To complicate the matter further, state-of-the-art calculations presently do not reproduce the upward bending of the carboxylic oxygen atoms on Cu(111), but show the Ag-like distortion pattern instead [16]. Nothing is therefore known about the possible origin of the contrasting behaviors on the Ag surfaces and the Cu(111) surface. Clearly, this calls for additional experiments.

In this paper we present a detailed study of the structure of the PTCDA/Cu(100) interface, based on the normal incidence x-ray standing wave (NIXSW) technique. The choice of the Cu(100) surface was motivated as follows: firstly, experiments on an additional Cu surface will reveal whether the distortion motif of Cu(111) is an exceptional or a more general property of Cu surfaces as such. Secondly, having a work

*Corresponding author: s.weiss@fz-juelich.de

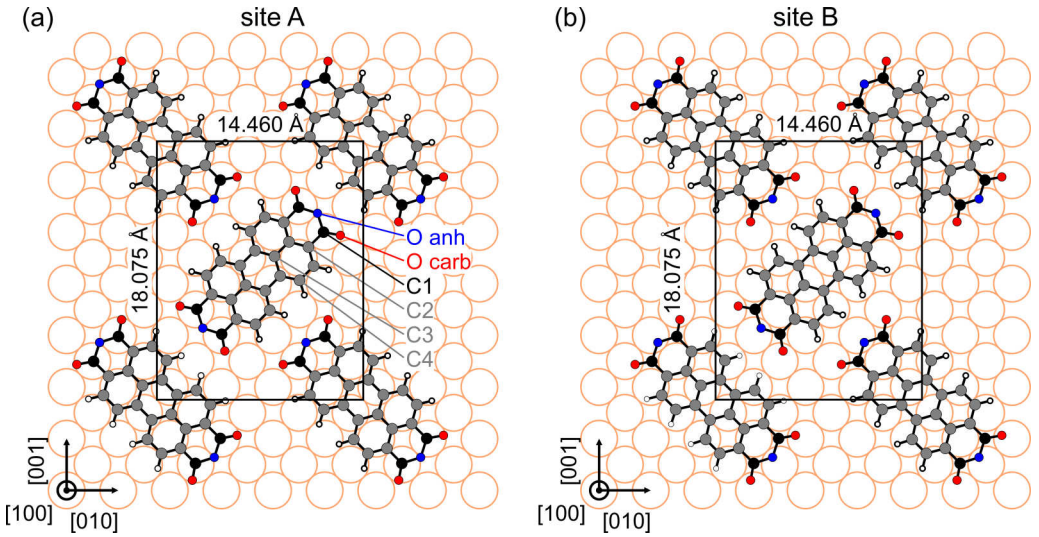

FIG. 1. Hard sphere models illustrating the two possible adsorption sites A and B of PTCDA on Cu(100) according to Gärtner *et al.* [17]. The chemical species that can be distinguished by XPS are marked by different colors: carboxylic oxygen—red, anhydride oxygen—blue, functional carbon C1—black, and perylene core: C2, C3, C4—gray. We note ahead that site B is confirmed by the reported experiment.

function of $\Phi_{\mathrm{Cu(100)}} = 4.59\,\mathrm{eV}$ [18], Cu(100) fills the gap between the work functions of Ag(111) ($\Phi_{\mathrm{Ag(111)}} = 4.40\,\mathrm{eV}$) [14] and Cu(111) ($\Phi_{\mathrm{Cu(111)}} = 4.90$ eV) [19]; the present experiment therefore provides an additional test probing the correlation of h^{vdW} and the work function. Moreover, this experiment may yield information how the work function and the distortion motif are related. Thirdly, the question whether PTCDA stays intact or decomposes upon adsorption on Cu(100) was controversially discussed in the literature [17,20,21]; our experiment should be able to resolve this issue unambiguously.

Data regarding the lateral interface structure of PTCDA on Cu (100) already exist from a detailed low-energy electron diffraction (LEED) and scanning tunneling microscopy (STM) study by Gärtner *et al.* [17]. A rectangular commensurate superstructure unit cell containing two molecules was found. The presence of a glide plane detected by LEED is compatible with two adsorption sites only. The NIXSW technique allows us to determine not only the vertical adsorption heights but also the lateral adsorption structure, if triangulation involving two separate Bragg reflections is carried out [10,11,22]. The two structures resulting from the two possible sites suggested by Gärtner *et al.* are shown in Fig. 1. In both cases, the center of the molecule is located above a bridge site. Both adsorption sites differ by a lateral shift of half a substrate lattice vector in [010] or [001] direction. For both adsorption sites, the long molecular axis is oriented parallel to the close-packed Cu rows of the surface, for site A (B) it falls between (on top of) the rows. Notably, for site A, most oxygen and carbon atoms, except the functional carbons labeled C1, are close to bridge or hollow sites. In contrast, for site B, the majority of atoms is found close to on-top positions. Whether site A or B is formed will therefore reveal details about the interaction mechanisms at the PTCDA/Cu(100) interface, and possibly at PTCDA/Cu interfaces in general.

II. EXPERIMENTAL DETAILS

The Cu(100) crystal was prepared by several sputter and annealing cycles. The cleanliness of the surface was controlled by measuring XPS spectra of the O 1*s* and C 1*s* core levels and LEED was used to verify the structure of the surface. PTCDA was evaporated from a home-built effusion cell onto the heated (400 K) Cu(100) surface at a residual pressure of 1.1×10^{-9} mbar. Gärtner *et al.* observed that molecular layers deposited at room temperature and at 400 K exhibit the same structure, but the deposition at room temperature leads to smaller domains which are separated by misfit areas with a slightly deviating structure [17]. This causes a broadening of the LEED spots. Although we deposited PTCDA onto a Cu(100) surface at 400 K, we observed a similar broadening as Gärtner et al. for deposition at room temperature [17]. This means that the structural order of our layer was of slightly lower quality than expected. Nevertheless, we expect that the present results are also meaningful for the ideal commensurate long range ordered structure of PTCDA/Cu(100) and that the disorder only affects the coherent fractions. During the sample preparation the PTCDA flux was monitored by measuring the ion current of the PTCDA fragment at $m/Z = 124$ amu using a mass spectrometer. The submonolayer coverage was concluded from the following facts: (1) LEED shows only diffraction spots associated with the first monolayer. This consists of flat lying molecules [17]. (2) Additional peaks in the C1s spectrum, which are observed for multilayers, were not detectable.

The NIXSW experiments were performed at the beamline I09 of Diamond Light Source under ultra high vacuum conditions. The experimental geometries are sketched in Fig. 2. In this geometry, the x-ray beam is *p*-polarized. A fluorescent screen is employed to monitor the intensity of the reflected beam. To hit this screen, the sample is tilted slightly out of

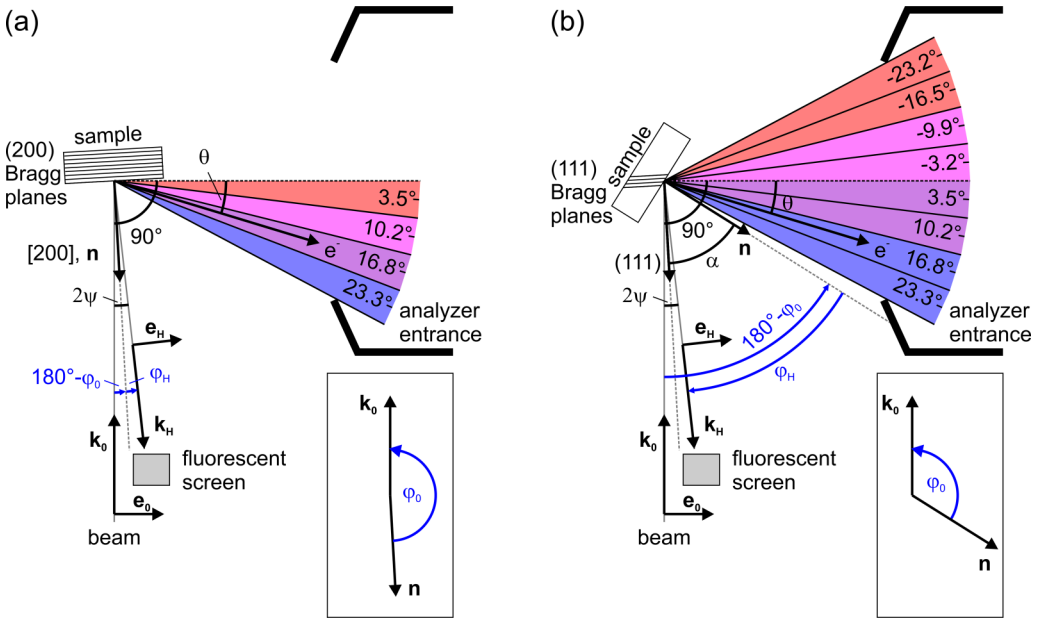

FIG. 2. Geometry of the NIXSW experiment on PTCDA/Cu(100). (a) (200) reflection. The surface normal $\vec{n}$ and hence the [200] vector is tilted by $\psi = 3.2^\circ$ against the incident x-ray beam with wave vector $\vec{k}_0$. The angle between incident and reflected x-ray beams is therefore $2\psi = 6.4^\circ$. θ is the angle between the direction of the emitted photoelectron and the direction of the incident x-ray polarization vector $\vec{e}_0$. It determines the nondipolar correction parameters Q_h and Q_0 [see Eqs. (A4) and (A5)]. φ_0 and φ_H are defined as the angles between $\vec{k}_0$ and $\vec{k}_H$, respectively, and the surface normal $\vec{n}$. They amount to $\varphi_0 = 180^\circ - \psi = 176.8^\circ$ and $\varphi_H = \psi = 3.2^\circ$. φ_0 and φ_H are used to calculate the b parameter [see Eq. (3)]. (b) (111) reflection. The surface normal $\vec{n}$ and the normal vector [111] on the (111) Bragg plane include an angle of $\alpha = 54.7^\circ$. The [111] vector is tilted by $\psi = 3.2^\circ$ against the incident x-ray beam. Hence $\varphi_0 = 180^\circ - (\alpha + \psi) = 122.1^\circ$ and $\varphi_H = \psi - \alpha = -51.5^\circ$.

the normal incidence geometry, resulting in a Bragg angle of $90^\circ - \psi \approx 86.8^\circ$. The beamline is equipped with a VG Scienta EW4000 analyzer. The optical axis of the analyzer is oriented at an angle of 90° with respect to the incident beam and parallel to $\mathbf{e}_0$. All NIXSW measurements were performed at room temperature with an analyzer pass energy of 200 eV yielding high signal intensities.

To triangulate the adsorption site, NIXSW measurements were performed with two different Bragg reflections. For the (200) reflection at a Bragg energy of $E_{\mathrm{Bragg}}^{(200)} = 3.4319$ keV, the sample normal $\mathbf{n}$ is nearly antiparallel to the x-ray beam $\mathbf{k}_0$ and nearly perpendicular to the electron analyzer [Fig. 2(a)], while for the (111) reflection at a Bragg energy of $E_{\mathrm{Bragg}}^{(111)} = 2.9721$ keV the surface normal is tilted by $\alpha = 54.74^\circ$ towards the analyzer [Fig. 2(b)].

At the (200) reflection, three XSW measurements were performed for the C 1s core level and two for the O 1s core level. For each core level, one XSW spectrum was measured at the (111) reflection.

XPS spectra were measured at $E_{\mathrm{photon}} = 3.4390$ keV for O 1s and C 1s core levels in order to clarify the chemical state of the PTCDA molecule in the monolayer on Cu(100) and to develop fitting models for the subsequent NIXSW analysis. This photon energy is chosen 7.1 eV above the Bragg energy $E_{\mathrm{Bragg}}^{(200)}$ to avoid standing wave effects. We also checked for beam damage by measuring the O 1s core level repeatedly. During 26 min, we observed an intensity decrease of 4.5% and 0.5% for the carboxylic oxygen and the anhydride oxygen peak, respectively, possibly indicating a small photoinduced loss of the carboxylic oxygen. In order to avoid significant beam damage, we restricted our NIXSW sequences for C 1s to 25 min. However, due to the low surface density of the oxygen species and their small photoemission cross-section at the photon energy corresponding to the Bragg conditions, the signal-to-noise ratio of the XPS spectra is poor. Therefore, for the O 1s NIXSW measurements, we increased the acquisition time to 45 min providing better XPS statistics. As a check we conducted 25-min- and 45-min-long NIXSW measurements for C 1s. Independent analysis of these data sets did not show any noticeable differences, proving that the influence of the beam damage is limited.

III. RESULTS

A. Off-Bragg core level spectroscopy

Figure 3 shows photoemission (PE) spectra of the O 1s and C 1s core levels at an off-Bragg photon energy of 3.439 keV. These are used to develop a fitting model for the NIXSW analysis. The O 1s spectrum [Fig. 3(a), Table I] can be well fitted with two doublets, an additional satellite peak, and a linear background. The doublets belong to carboxylic oxygen (O carb, $E_{\mathrm{b}}^{\mathrm{O\,carb}} = 531.63$ eV, $E_{\mathrm{b}}^{\mathrm{O\,carb\,sat}} = 533.59$ eV) and to anhydride oxygen (O anh, $E_{\mathrm{b}}^{\mathrm{O\,anh}} = 533.98$ eV, $E_{\mathrm{b}}^{\mathrm{O\,anh\,sat}} = 535.94$ eV). Both doublets consist of a main peak and a satellite at higher binding energy, which is in accordance with previous fitting models for PTCDA on differently oriented Ag surfaces [10–12]. The satellites can be attributed to shakeup processes [23]. The intensity ratio between the integrated peak areas of carboxylic and anhydride oxygen agrees well with the 2:1 stoichiometry of the intact PTCDA molecule. This supports a nondissociative adsorption of PTCDA on Cu(100), in contrast

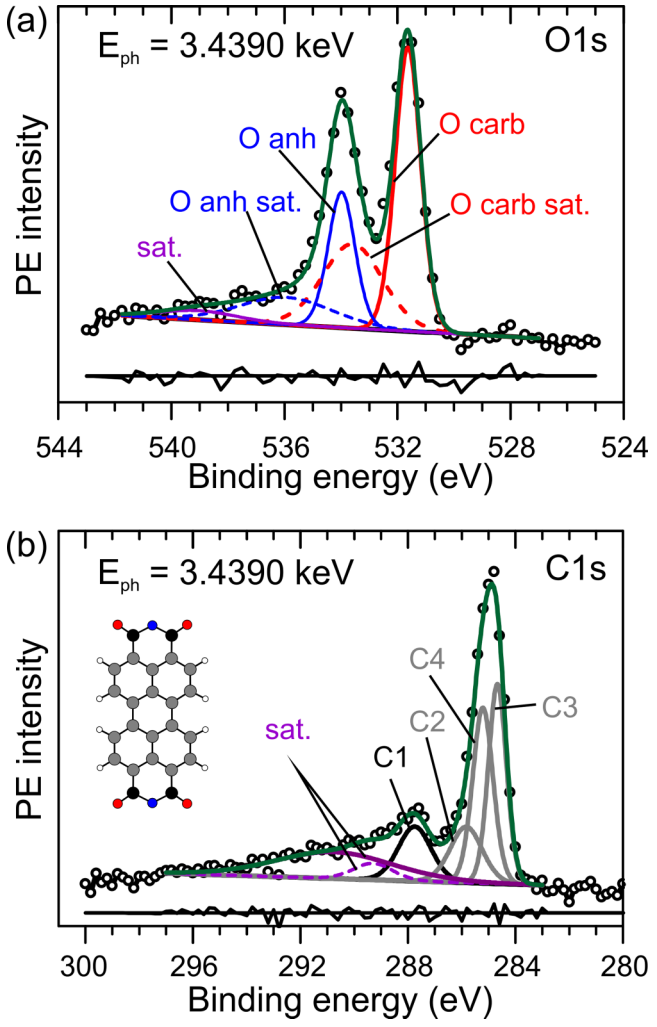

FIG. 3. Off-Bragg photoemission spectra (black open dots) measured at 3.4390 keV photon energy and corresponding fitting models: (a) the photoemission spectrum of the O 1*s* core level was fitted by five peaks: main peak of carboxylic oxygen (red), its satellite (red, dashed), main peak of anhydride oxygen (blue), its satellite (blue, dashed), an additional satellite (purple) and a linear background. The fit is depicted in green. (b) Six peaks are used to fit the PE signal of the C 1*s* core level. C3, C4, C2 (gray), and C1 (black) are the main peaks of the different carbon species. Two satellites (purple) and a linear background are introduced. The green line shows the fit. The inset shows the PTCDA molecule, using the respective colors for the different chemical species.

to the findings of Refs. [20] and [21], but in accordance with Ref. [17].

To describe the C 1*s* XPS spectra [Fig. 3(b), Table I], an existing fitting model was adapted [12,23]. The signal consists of contributions from the functional carbon atoms (C1) and the different species of the carbon backbone [C2, C3, C4; see Fig. 1(a) for notation] and two additional not further resolved satellites. The peak positions of the different carbon species are $E_b^{C3} = 284.67$ eV, $E_b^{C4} = 285.21$ eV, $E_b^{C2} = 285.83$ eV, and $E_b^{C1} = 287.75$ eV. For the fitting of the spectra, the total photoemission intensities of the separate peaks were constrained as follows: $I_{C1} = I_{C2} = 0.5I_{C3} = 0.5I_{C4}$. In this way, the correct stoichiometry of PTCDA was safeguarded.

B. NIXSW using the (200) reflection

The NIXSW technique was reviewed in several publications [24–27]. In each of our NIXSW experiments, a set of PE spectra was measured at photon energies varying by approximately ±3 eV around the Bragg energy. To extract partial PE yield curves, i.e., the integrated intensities of the corresponding PE peaks as a function of photon energy, fitting models developed from off-Bragg PE spectra (Fig. 3) were applied. Specifically, the peak positions of the components and their full widths at half maximum (FWHM) were constrained in accordance with the corresponding fitting models, while the intensities were taken as free fitting parameters.

In the case of oxygen, the relative intensities of the satellite peaks were constrained with respect to the intensities of the corresponding main peaks, according to the off-Bragg fitting model. For carbon, it was not possible to differentiate the partial contributions of C2, C3, and C4 from each other, because the given signal intensity did not allow a better energy resolution. Therefore, we carried out a differential analysis for the C1 component only, but added the contributions of C2, C3, and C4. Examples for the resulting PE yield curves for C1, C2+C3+C4, O carb, and O anh are shown in Fig. 4. The error bars were determined as described in Ref. [28].

NIXSW data are commonly analyzed in the framework of the dipole approximation for the photoemission process. In the dipole approximation, the angular distribution of the photoelectrons has a forward-backward symmetry with respect to the propagation direction of the electromagnetic radiation. Thus, in this approximation, incident and reflected x-ray beams in NIXSW yield the same angular photoelectron distribution. However, beyond the dipole approximation, this symmetry is

TABLE I. Binding energies (E_b), FWHM and the relative peak area of the different components of the C 1*s* and O 1*s* spectrum as displayed in Fig. 3 measured at 3.4390 keV photon energy. For the C 1*s* spectrum the satellites can not be attributed to a specific main peak.

Peak	E_b(eV)	FWHM (eV)	Area(%)	Peak	E_b (eV)	FWHM (eV)	Area (%)
C1	287.75	1.50	12.3	O carb	531.63	1.11	38.0
C2	285.83	1.46	12.3	O carb sat.	533.59	2.59	26.3
C3	284.67	0.82	24.7	O anh	533.98	1.16	19.0
C4	285.21	0.94	24.7	O anh sat.	535.94	4.02	13.1
sat. 1	289.30	1.79	4.5	sat.	539.05	3.36	3.7
sat. 2	290.77	5.36	21.5				

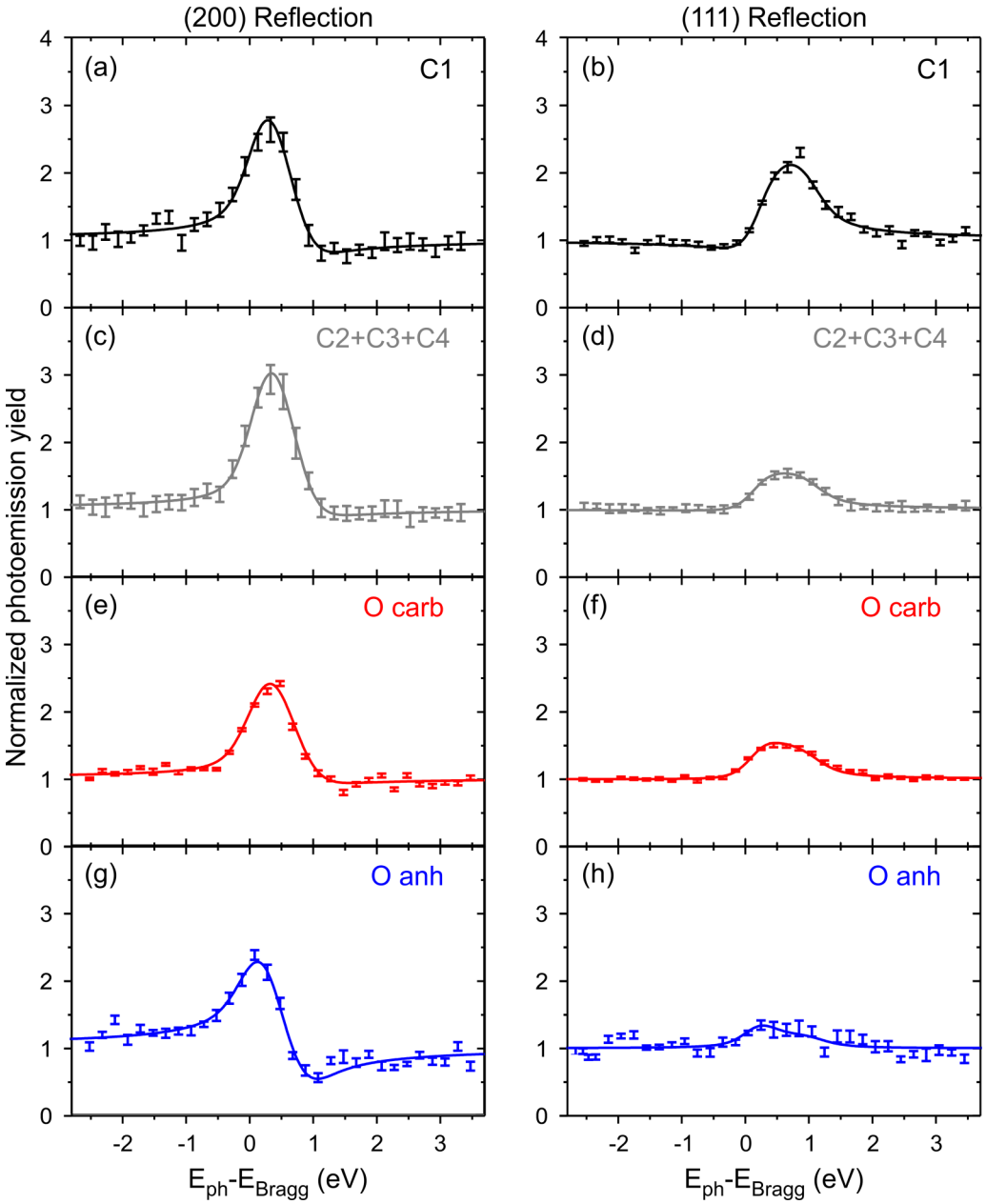

FIG. 4. Partial photoemission yield vs photon energy relative to Bragg energy for the (200) reflection (left) and the (111) reflection (right) for different chemical species and fitted yield curves. The data were taken from the angular slice providing the highest intensity, with a central angle $\theta = 73.2^\circ$ for (200) reflection and $\theta = 109.9^\circ$ for (111) reflection. Symbols indicate experimental partial yields including error bars.

broken, with the result that in the backscattering geometry the reflected beam contributes stronger to the recorded photoemission yield than the incident beam. Unless the photoelectrons are detected exactly perpendicular to incident and reflected beams, hence for perfect normal incidence, this requires a correction of the dipolar NIXSW analysis [29,30]. Hence, in the present experimental geometries (Fig. 2), nondipolar corrections need to be (and have been) taken into account for two reasons: (1) because of the small tilt ψ of the sample, the reflected beam is tilted by 2ψ relative to the analyser axis. This introduces the need for nondipolar corrections even for photoelectrons that are emitted along the analyzer axis (i.e., perpendicular to the incident, but not the reflected, x-ray beam) [31]. (2) Because the acceptance angle of the analyzer is large (in the present experiment this angle is $\pm 30^\circ$), the majority of the detected photoelectrons includes angles $\neq 90^\circ$ with the incident and reflected x-ray beams, requiring a correction for nondipolar effects that cannot be neglected. As illustrated in Fig. 2, we have carried out this correction for angular slices of approximately 7° width separately, because the nondipolar correction parameters depend on the angle θ between the emission direction of the photoelectrons and the polarization direction of the (incoming) x-ray beam.

In the dipole approximation with nondipolar corrections, the partial PE yield is given by [30]

$$Y^i = 1 + S_R R + 2|S_I|\sqrt{R} F_c^i \cos\left(\phi - 2\pi P_c^i + \Psi\right). \quad (2)$$

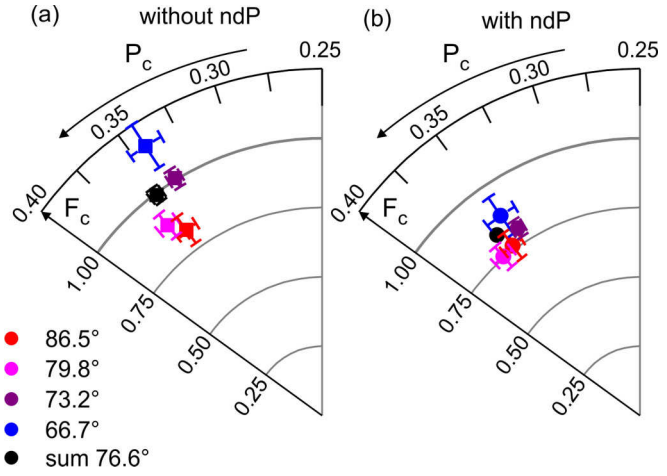

FIG. 5. Argand diagrams showing coherent positions and coherent fractions determined for the carbon backbone (C2+C3+C4) from one single experiment using the (200) reflection. Coherent positions and coherent fractions determined from different angular detector slices are indicated by different colors. The fits were performed without (a) and with (b) nondipolar correction. Without the nondipolar correction some coherent fractions are greater than unity, which is unphysical. The nondipolar correction reduces the spread in coherent fractions and increases coherent positions slightly. The quoted angles θ are measured between the incoming x-ray beam and the central PE detection angle for the corresponding slice on the detector. For the data point labeled "Sum," the PE signal was integrated across the entire acceptance angle of the analyser and the mean angle was used to calculate the nondipolar correction parameters. Error bars that are smaller than the corresponding data point were omitted for clarity.

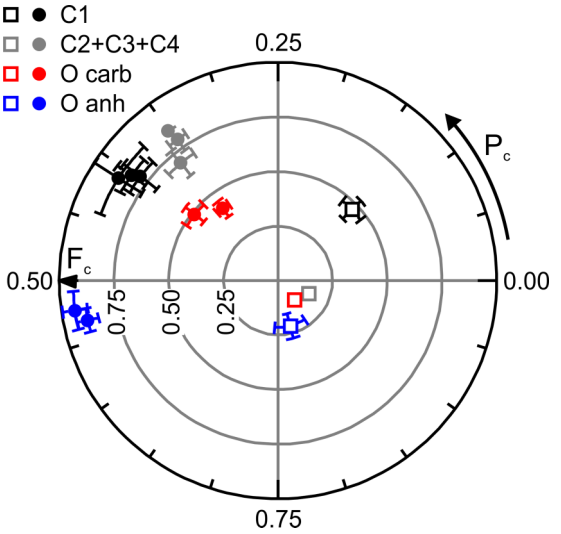

FIG. 6. Argand diagram showing coherent positions and coherent fractions averaged over all slices for the (200) reflection (solid dots) and the (111) reflection (open squares) for different chemical species indicated by different colors.

The coherent positions P_c^i and coherent fractions F_c^i of species i specify its position and spread; and S_R, $|S_I|$, Ψ are the nondipolar correction parameters. They can be calculated from the angular distribution parameter γ and the scattering phase shifts δ_p, δ_d for p- and d-asymptotic waves. γ was calculated in the framework of the quadrupole approximation by Trzhaskovskaya and tabulated as a function of the photon energy [32]. The values of γ corresponding to our experimentally used photon energies were calculated by linear interpolation of the tabulated values. δ_p and δ_d were taken from the NIST Electron Elastic-Scattering Cross-Section Database, Version 3.2 [33]. Further details are given in Appendix A.

To extract the coherent position of atomic species C1, C2+C3+C4, O carb and O anh relative to the (200) Bragg planes, the data in Fig. 4 (left column) (and equivalent data for other slices) were fitted by Eq. (2). The lines in Fig. 4 show these fits. They have been generated with the program TORRICELLI [34], using P_c^i and F_c^i as free fitting parameters while fixing S_R, $|S_I|$, Ψ to the values shown in Table V. The importance of the nondipolar correction parameters in the present case of an analyzer with large acceptance angle is illustrated in Fig. 5 for the example of the C2+C3+C4 component. It has been shown generally that the neglect of nondipolar effects leads to artificially large coherent fractions [35]. This is also apparent in the Argand diagram of Fig. 5(a), in which the coherent positions and fractions resulting from the fits of PE yield curves in different angular slices without nondipolar corrections are plotted. For $\theta \gtrsim 15°$, the coherent fractions are indeed larger than 1. In fact, as we move away from $\theta \simeq 0$, where nondipolar corrections are small, F_c increases steadily. This is the result of progressively stronger deviations from the dipole approximation. After proper correction for nondipolar effects, one expects the Argand vectors of different angular slices to coincide, as indeed they do [Fig. 5(b)]. The correction leads to slightly increased positions, in accordance with findings concerning the impact of the nondipolar correction parameters [26].

Having separated the PE yield into angular slices in order to carry out the θ-dependent nondipolar correction, we now need to calculate coherent positions and fractions that represent the averages from the results for the individual slices. This is done by a weighted vector sum; details are given in Appendix B.

The final NIXSW results for the (200) reflection for components C1, C2+C3+C4, O carb and O anh of several independent experimental data sets, recorded on Cu(100), are presented in the Argand diagram in Fig. 6. The corresponding averages over all experiments are given in Table II. We note that the coherent fractions are high, which proves a

TABLE II. Averaged coherent positions and fractions of the different chemical species for the (200) reflection and the (111) reflection. The adsorption height is given by $h_{200}^i = (1 + P_c^i)d_{200}$.

	O carb	O anh	C2+C3+C4	C1
		(200) reflection		
P_c^i	0.37 ± 0.03	0.53 ± 0.01	0.35 ± 0.01	0.40 ± 0.01
F_c^i	0.43 ± 0.07	0.91 ± 0.04	0.82 ± 0.08	0.82 ± 0.06
h_{200}^i(Å)	2.47 ± 0.05	2.76 ± 0.02	2.44 ± 0.02	2.53 ± 0.02
		(111) reflection		
P_c^i	0.86 ± 0.03	0.79 ± 0.07	0.94 ± 0.03	0.12 ± 0.03
F_c^i	0.13 ± 0.02	0.22 ± 0.06	0.15 ± 0.02	0.47 ± 0.06

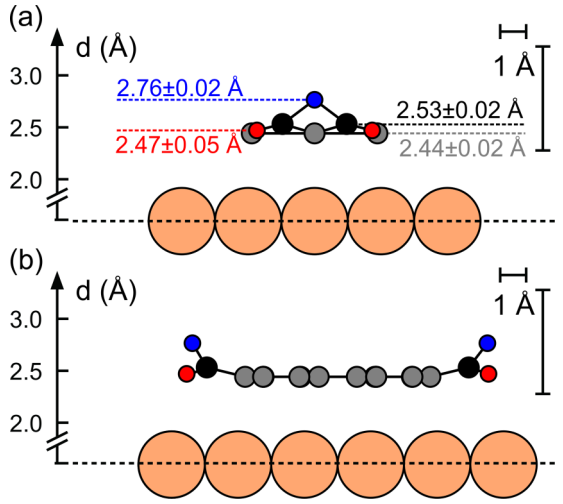

FIG. 7. Hard sphere model of the PTCDA/Cu(100) interface in side view projection along the long (a) and short (b) molecular axes. The heights are taken from Table II. The Cu surface layer is positioned at the outermost Bragg planeas extrapolated from the bulk, thus disregarding any possible surface relaxation. The radii of the carbon and oxygen atoms in PTCDA as plotted correspond to half of their covalent radii; the color coding corresponds to Fig. 1. Note that the vertical scale of the molecule is expanded by a factor of 4.

good vertical order in our molecular films. Calculating the adsorption heights from the coherent positions is done by using $h^i_{200} = (n + P^i_c)d_{200}$ with an integer value n. For $n = 1$ and $d_{200} = 2.6147$ Å at 293 K [36], physically reasonable heights of (2.47 ± 0.05) Å for O carb, (2.76 ± 0.02) Å for O anh, (2.44 ± 0.02) Å for C2+C3+C4, and (2.53 ± 0.02) Å for C1 are obtained.

Figure 7 shows a hard sphere model of the vertical adsorption geometry of PTCDA on Cu(100). In contrast to the gas phase, the adsorbed molecule is not planar. We find the C1 and carboxylic oxygen atoms 0.09 and 0.03 Å above the carbons C2+C3+C4 (carbon backbone), but we have to point out that the second value is still in the range of experimental uncertainty. In contrast, the anhydride oxygen is located considerably higher, i.e., 0.32 Å above the carbon backbone.

C. NIXSW using the (111) reflection

In order to triangulate the lateral position of the molecule on the Cu(100) surface, it is necessary to carry out NIXSW measurements on at least one additional set of lattice planes. For symmetry reasons, we have chosen the set of (111) planes. Conceptually, the experiment and the analysis were carried out in precisely the same way as for the (200) reflection, with two exceptions: firstly, adjacent pairs of angular slices [cf. color-coding in the Fig. 2(b)] were summed before extracting the PE yield, in order to optimize signal intensity. Secondly, the different experimental geometry displayed in Fig. 2(b) with the large angle $\alpha + \psi$ between the incident x-ray beam and the surface normal of the sample changes the width of the reflectivity curve. This is parametrized by the b parameter [37]

$$b = \frac{\cos(\varphi_0)}{\cos(\varphi_H)} = \frac{\cos(180^\circ - (\alpha + \psi))}{\cos(\psi - \alpha)} = -0.85. \quad (3)$$

Uncertainties of $\pm 0.5^\circ$ in the incidence angle $\alpha + \psi$ yield a variation of b by ± 0.02. The corresponding uncertainties in P_c and F_c have been included in their error bars. For the geometry in Fig. 2(a), where α is zero and the normal to the Bragg planes coincides with the normal to the surface, one obtains $b = -1$. The nondipolar correction parameters for the (111) reflection at $E^{(111)}_{\text{Bragg}} = 2.9721$ keV are given in Tables IV and V.

Representative PE yield curves recorded for the (111) reflection and the corresponding fits are shown in Fig. 4 (right column), an Argand diagram including the results from all recorded data sets is displayed in Fig. 6, and the averaged values for the coherent positions and the coherent fractions are given in Table II. Compared to the results for the (200) reflection the coherent fractions of all species are noticeably reduced, by a factor of ≈4, except for the C1 species where the factor is only 1.7. This reduction is explained by the fact that photoemitters within one PTCDA molecule are located in positions that lack commensurability to the Cu(001) lattice. As a consequence, both carbon and oxygen species are located at several different distances from the (111) Bragg planes. This is illustrated in Fig. 8. Hence, the experimentally determined P_c and F_c originate from a superposition of photoemitters at different distances to (111) Bragg planes. This reduces significantly the coherent fractions, except for the C1 species where accidentally all atoms have a similar distance to the (111) planes.

D. Determination of the adsorption site

The principle of triangulation is sketched in Fig. 8. A NIXSW experiment furnishes the orthogonal distance a_{hkl} between a set of equivalent photoemitters and a set of Bragg planes. Hence an NIXSW experiment with reflections on the hkl family of Bragg planes defines a plane E_{hkl} in which the photoemitters must be located. Examples of such planes are indicated by dashed lines in Fig. 8. Evidently, three inequivalent, nonparallel hkl reflections are required for the precise location of an adsorbed species by NIXSW triangulation. The point in which the three planes E_{hkl} intersect is the adsorption site [11]. Generally, if additional symmetry constraints exist, only two specifically chosen reflections may be sufficient [26]. Fortunately, the superstructure of PTCDA on Cu(100) exhibits two perpendicular glide planes, which restrict the number of possible adsorption sites to two. Therefore we can determine the site of the molecule using only the (200) and (111) reflections.

A problem with this direct form of triangulation arises when equivalent photoemitters occupy different adsorption sites, because in this case the NIXSW experiments provide only the average distance $\bar{a}_{hkl}$ with respect to a given set of Bragg planes and this prevents the direct triangulation of the inequivalent adsorption sites. Therefore an additional analysis is required. The present case of PTCDA/Cu(100) belongs to this class, since its superstructure unit cell (Fig. 1) contains several atoms, labeled j_i, of each distinguishable species i ($j_i = 1, \ldots, m_i$ with $m_i = 8$ for the eight functional carbon atoms, and similarly for the four anhydride oxygen atoms, eight carboxylic oxygen atoms, and the 40 atoms of the carbon backbone).

The approach taken in the present case is to calculate expected coherent positions and fractions with respect to the

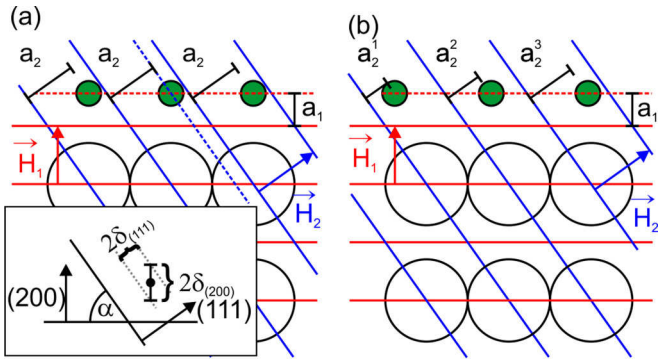

FIG. 8. Principles of triangulation, sketched in 2D projection. (a) If the adsorbed atoms of a given species (green circles) are in commensurate registry with the substrate (large black open circles), direct triangulation is possible. The intersection of sets of planes E_{hkl} of possible positions (dashed lines) defined for each Bragg reflection $\mathbf{H}_s = (hkl)$ (solid lines) yields the adsorption site of the adsorbate. The inset shows the influence of disorder perpendicular to the $\mathbf{H}_1 = (200)$ plane on the disorder perpendicular to the $\mathbf{H}_2 = (111)$ plane. (b) If adsorbate atoms of the same species occupy different adsorption sites within a bigger commensurate superstructure unit cell, the distance to the inclined Bragg planes $\mathbf{H}_2$ varies from atom to atom. In that case, the coherent position is defined by a vector sum over all atoms of the given species within the superstructure unit cell.

(111) Bragg planes for the two different adsorption sites A and B in Fig. 1 and to compare them with the experimental result for the (111) reflection in Table II. This requires the knowledge of all atom positions within the PTCDA layer.

To obtain the atom positions within the PTCDA molecule, we performed a DFT calculation of the free molecule, employing Gaussian [38] and used the thus calculated lateral atomic coordinates (x,y) within the molecule in conjunction with the adsorption heights h^i_{200} from Table II to obtain the complete (x,y,h^i_{200}) coordinates of all atoms in the PTCDA molecule. Then, we placed two PTCDA molecules in the PTCDA/Cu(100) superstructure unit cell and arranged the PTCDA layer on the Cu(100) surface such that molecules sit either in site A or B (Fig. 1). For each of the two structure models, this provides the coordinates $\mathbf{r}^{i,j_i}$ of each atom j_i of species i inside the superstructure unit cell. We remark that this approach neglects lateral relaxations within the molecule, which occur upon adsorption. We also note that in the following adsorption site analysis, only the four anhydride oxygen, eight carboxylic oxygen, and eight functional carbon atoms within the superstructure unit cell are considered [compare Fig. 9(a)]. In the remainder of this section, symbols P_c and F_c for various coherent positions and fractions always refer to the (111) reflection, unless stated otherwise.

The distance between atom i,j_i and the (111) plane is given by

$$a^{i,j_i}_{(111)} = \mathbf{r}^{i,j_i} \cdot \mathbf{n}, \quad \mathbf{n} = \frac{1}{\sqrt{3}}\begin{pmatrix}1\\1\\1\end{pmatrix}. \tag{4}$$

Equation (4) is illustrated for the three relevant species in Figs. 9(b)–9(d), showing projections of the PTCDA/Cu(100) superstructure unit cell onto the $(01\bar{1})$ plane for the case of adsorption site B. Considering the anhydride oxygen atoms in Fig. 9(b) as an example, it becomes obvious that the distances between the adsorbate atoms and the Bragg planes (indicated by dashed lines), and hence also the respective coherent positions

$$P^{i,j_i}_c = \frac{a^{i,j_i}_{(111)}}{d_{(111)}} \bmod 1, \tag{5}$$

may vary strongly within one species i. For each atom i,j_i its Argand vector $(P^{i,j_i}_c, F^{i,j_i}_c)$, with $F^{i,j_i}_c = m_i^{-1}$, is displayed in the Argand diagram in Fig. 9(e). m_i is the number of atoms

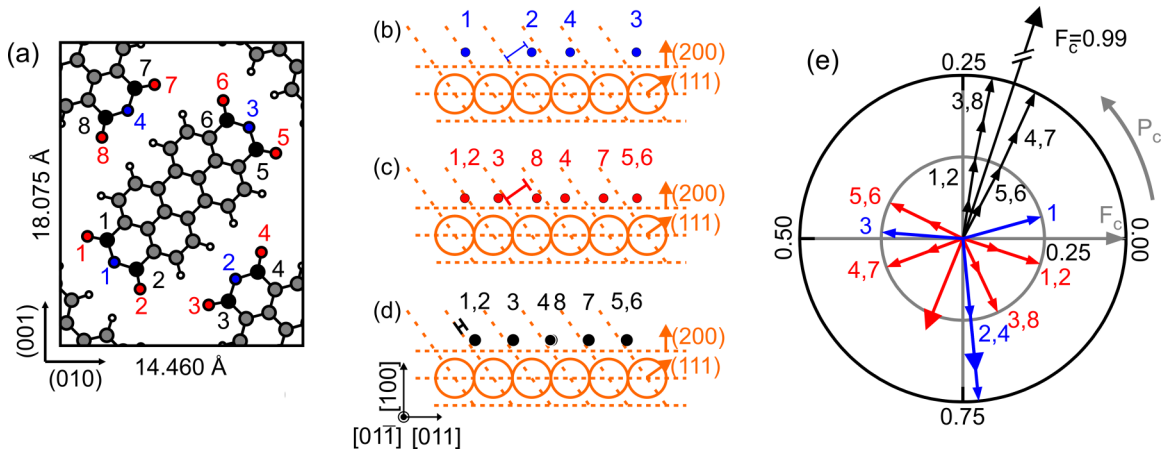

FIG. 9. (a) Superstructure unit cell of PTCDA/Cu(100). The four anhydride oxygen atoms (blue), eight carboxylic oxygen atoms (red), and eight functional (C1) carbon atoms (black) in the superstructure unit cell are labeled. (b)–(d) Projections of the PTCDA/Cu(100) superstructure unit cell in adsorption site B onto the $(0\bar{1}1)$ plane for anhydride oxygen (b), carboxylic oxygen (c) and functional carbon (d). Atoms are labeled according to (a) and the vertical distances of the chemical species from the (200) planes are taken from Table II. If several atoms share the same projected position, their numbers are separated by a comma. For the functional carbon species, atoms 4 and 8 have nearly the same distance to the (111) plane. (e) Argand diagram showing the coherent positions of the atoms plotted in (b)–(d). The fractions are $1/m_i$. Arrows with large heads indicate the vector sum for each type of species. The gray (black) circle indicates a coherent fraction of 0.25 (0.5).

of the chemical species i within the superstructure unit cell. The overall coherent positions P_c^i and coherent fractions $F_{c,0}^i$ of species i can be calculated by the vector sum

$$\tilde{f}_{c,0}^i \equiv F_{c,0}^i \, e^{2\pi i P_c^i} = \frac{1}{m_i} \sum_{j_i=1}^{m_i} \tilde{f}_c^{i,j_i}, \tag{6}$$

where $\tilde{f}_c^{i,j_i} \equiv F_c^{i,j_i} e^{2\pi i P_c^{i,j_i}}$ as also indicated in Fig. 9(e).

Using Eqs. (4) to (6), we obtain for adsorption site B, $P_c^{O\,anh} = 0.765 \pm 0.004$, $P_c^{O\,carb} = 0.683 \pm 0.014$ and $P_c^{C1} = 0.200 \pm 0.006$, while for site A, we get $P_c^{O\,anh} = 0.265 \pm 0.004$, $P_c^{O\,carb} = 0.183 \pm 0.014$ and $P_c^{C1} = 0.700 \pm 0.006$. The error bars of P_c^i were determined by error propagation from the error bars of the heights $h_{(200)}^i$ (cf. Table II). The coherent fractions $F_{c,0}^i$ are the same for adsorption site A and B ($F_{c,0}^{O\,anh} = 0.413$, $F_{c,0}^{O\,carb} = 0.303$, and $F_{c,0}^{C1} = 0.990$). We remark that the coherent fractions $F_{c,0}^i$ are ideal coherent fractions in the sense that they are based on the assumption of perfect lateral and vertical order in the molecular layer. However, the coherent fractions for the (200) reflection are smaller than unity. The corresponding vertical disorder will, in addition to any influence from lateral disorder, reduce the coherent fraction for the (111) reflection from its ideal value $F_{c,0}^i$ to F_c^i, as sketched in the inset of Fig. 8(a). The reduction through vertical disorder can be expressed by

$$F_c^i = F_{c,0}^i \sqrt[4]{F_c^i(200)}, \tag{7}$$

which is derived in Appendix C. Hence the ideal coherent fractions $F_{c,0}^i$ are reduced by factors of 0.98, 0.81, 0.95 for anhydride oxygen, carboxylic oxygen and C1, respectively, through vertical disorder. Lateral disorder will lead to further reductions.

In Fig. 10, the expected coherent positions P_c^i and fractions F_c^i for the (111) reflection, as calculated from Eqs. (6) and (7), are compared to the experimentally determined ones. Overall, the deviations between the calculated and experimentally determined coherent positions, indicated by the curved arrows, are significantly smaller for adsorption site B than for adsorption site A. For carboxylic oxygen, the deviation from the predicted values are large for both sites, but carboxylic oxygen has a low coherent fraction, hence the precise value of the coherent position is less meaningful. For C1, we obtain the highest coherent fraction and a small error bar. This result, which shows a clear preference for site B, is therefore the most meaningful one. We note that for anhydride oxygen and C1 the deviations between experimental and predicted coherent fractions for the adsorption site B are in the typical precision range of NIXSW experiments.

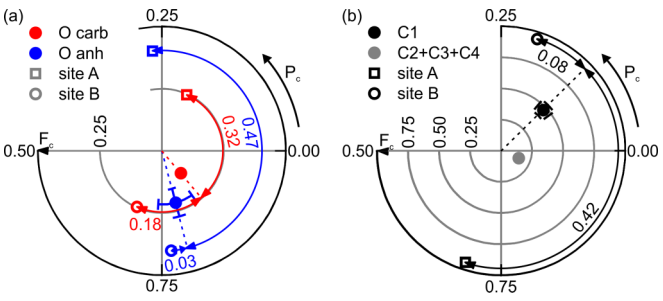

FIG. 10. Comparison between experimental and calculated coherent positions and fractions for oxygen (a) and carbon species (b) for the (111) reflection. Different chemical species are indicated by different colors, in accordance with the color code used throughout the paper. Solid symbols indicate experimental results and open symbols the calculated data for the two different adsorption sites A (squares) and B (circles). If error bars are of a size that is comparable to the size of the data point itself, they are omitted for clarity. The curved arrows and corresponding numbers indicate deviations between the experimental coherent positions and the corresponding ones from calculations for sites A and B. Note the different radial scales of the Argand diagrams in (a) and (b).

Based on the above analysis, we conclude that adsorption site B is the correct one. Possible reasons for the deviations of experimental coherent positions and fractions from the calculated ones for site B are the following: first, structural defects in the lateral order of the molecular layer. Second, in the experiment a small portion of molecules may in fact be adsorbed on site A. Third, the fact that the lateral coordinates of the free molecule were used in the analysis may yield systematic deviations of the calculated coherent positions from the correct ones for site B. The first two mechanisms reduce especially the experimental coherent fractions F_c^i. In contrast, the calculation of the expected coherent fractions F_c^i includes only the vertical, not the lateral disorder. This may explain why the experimental coherent fractions in Fig. 10 are considerably smaller than the calculated ones.

To confirm the above conclusion and to illustrate the accuracy of our site assignment, we repeated the adsorption site analysis in real space. Specifically, we calculated the set of all adsorption positions of the molecule that are consistent with the experimental results for the coherent position. To this end, we shifted the PTCDA layer with its correct supercell geometry rigidly across the Cu(100) surface (thereby ignoring our knowledge about the glide plane symmetry), calculating in each position the expected coherent position. Again, the

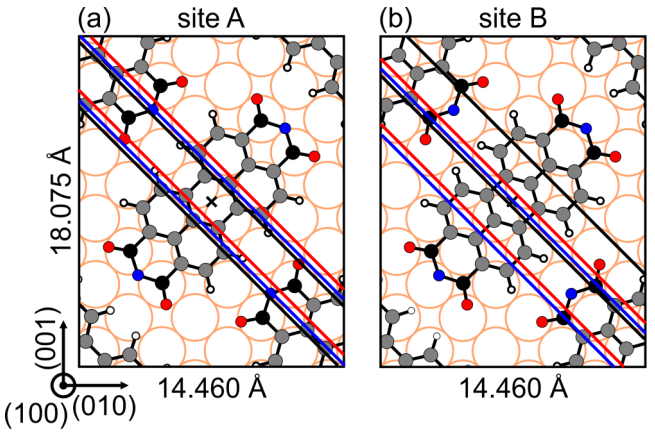

FIG. 11. Superstructure unit cell of PTCDA on Cu(100), plotted for adsorption sites A (a) and B (b). The colored lines, which are lattice periodic and identical in (a) and (b), indicate all positions of the molecular center (black cross) that are compatible with the coherent positions [(111) reflection] of the species of the corresponding color: anhydride oxygen—blue, carboxylic oxygen—red, and functional carbon (C1)—black. Evidently, adsorption site B is in agreement with experimental results.

TABLE III. Shortest lateral distances between the center of the molecule at adsorption sites A and B and the adsorption positions which are compatible with experiment, indicated by straight lines in Fig. 11. For the anhydride oxygen and functional carbon (C1) species, site B shows significantly shorter distances, while for the carboxylic oxygen species, the distances for both sites are rather higher (compare Fig. 11).

	site A	site B
O anh	1.21 Å	0.07 Å
O carb	0.82 Å	0.46 Å
C1	1.08 Å	0.20 Å

carboxylic oxygen, anhydride oxygen, and C1 signals were analyzed separately.

In Fig. 11, all adsorption sites of the center of the molecule that are consistent with experimental coherent positions are shown. The colors refer to the data that have been used in the analysis. For example, the black lines mark all adsorption sites that are consistent with the measured coherent position of C1. For reference, Fig. 11 also shows the locations of molecules in structural models A (panel a) and B (panel b). The red, blue and black lines in Figs. 11(a) and 11(b) are identical. For each data set the consistent sites are located on straight lines parallel to the (111) plane. This is evident, since shifting the molecules parallel to this plane does not change the distances of the atoms to it. The deviation between the red, black, and blue lines reveals a slight inconsistency of adsorption site assignments based on the three independent signals (carboxylic oxygen, anhydride oxygen, C1). The deviation of red, black, and blue lines from the center of the molecule corresponds to the $P_c^i(\mathrm{exp}) - P_c^i(\mathrm{calc})$ in the Argand diagrams of Fig. 10. It is clear that both the internal inconsistency and the deviation from site B is much smaller than the deviation from site A. It is therefore unambiguously clear that site B is not only compatible with experiment, but the agreement between site B and experiment is in fact very good.

To quantity this agreement, we turn to Table III, which shows the minimum lateral distance between the center of the molecule adsorbed at sites A and B and the lines of experiment-consistent sites. The values for site B reveal consistently smaller deviations from experiment, especially in the case of the anhydride oxygen. Nonetheless, the deviations are still greater than 0.05 Å that are considered to be the typical precision achievable in NIXSW experiments. The reason might be that the layer contained structural defects and misfit areas as mentioned before.

IV. DISCUSSION

We start our discussion by pointing out that our experiments clearly show that PTCDA on Cu(100) adsorbs as an intact molecule and that decomposition is possibly relevant only at higher temperatures.

In the following discussion, we disregard a possible relaxation of the Cu(100) surface. Instead, we use the outermost Bragg plane as extrapolated from the bulk of the substrate as reference for the PTCDA adsorption heights. For the clean Cu(100) surface, Davis and Noonan have reported relaxations of $\Delta d_{12} = -1.10\%$ and $\Delta d_{23} = +1.70\%$ [42]. This yields a small outwards relaxation of the top surface layer into the vacuum by 0.60% or 0.01 Å. While the relaxation of the PTCDA-covered Cu(100) surface is not known, we nevertheless expect it to be of similar size. Hence effects due to the substrate relaxation are presumed to be smaller than the experimental uncertainties of the adsorption heights above the extrapolated Bragg planes.

To put the vertical adsorption height and molecular distortion of PTCDA on Cu(100) into perspective, we plot the vdW-corrected vertical adsorption heights h^{vdW} of PTCDA on a range of coinage metal surfaces [4,5,8–12] in Fig. 12. In previous publications [9,14], we have used experimentally determined van der Waals radii $r_{\mathrm{Au}}^{\mathrm{vdW}} = 1.66$ Å, $r_{\mathrm{Ag}}^{\mathrm{vdW}} = 1.72$ Å, and $r_{\mathrm{Cu}}^{\mathrm{vdW}} = 1.40$ Å from x-ray diffraction and critical volumes [40] in this context. Corresponding vdW-corrected adsorption heights are shown in panel (a) of Fig. 12. Here, we complement these data by vdW-corrected adsorption heights that are based on theoretically calculated vdW radii [41] $r_{\mathrm{Au}}^{\mathrm{vdW}} = 1.54$ Å, $r_{\mathrm{Ag}}^{\mathrm{vdW}} = 1.36$ Å, and $r_{\mathrm{Cu}}^{\mathrm{vdW}} = 1.27$ Å [Fig. 12(b)]. The theoretical values for the vdW radii were used successfully to study the adsorption of PTCDA on Au(111) and Xe on various noble metal surfaces. They were calculated using the so-called DFT + $\mathrm{vdW}^{\mathrm{surf}}$ method [41]. These radii are 0.12, 0.36, and 0.13 Å smaller for Au, Ag and Cu, respectively, than the experimentally determined vdW radii of Ref. [40]. In spite of these differences, Figs. 12(a) and 12(b) reveal similar tendencies, and in the following we will only discuss common features which are seen for both curves.

We start the discussion of Fig. 12 by a remark concerning the interpretation of vdW-corrected adsorption heights. On Au(111) the vdW-corrected adsorption height amounts to—depending on the chosen vdW radius—from 1.61 to 1.73 Å, which agrees well with the vdW radius of carbon $r_{\mathrm{C}}^{\mathrm{vdW}} = 1.70$ Å [40]. This indicates a pure vdW interaction between the molecule and the Au(111) substrate. However, Fig. 12 shows as well that the vdW-corrected adsorption heights of the carbon backbone of PTCDA on all of the Ag and Cu surfaces are significantly smaller than $r_{\mathrm{C}}^{\mathrm{vdW}}$, indicating additional attractive interactions beyond van der Waals on all studied surfaces except Au(111).

In Introduction, we raised the question whether the bonding situation of PTCDA on Cu(111), with the oxygen atoms above the carbon plane, is unique. Figure 12 provides the answer. There are two aspects. First, the molecular distortion patterns for PTCDA on the Cu(111) and the Cu(100) surface are in fact similar in the sense that the carboxylic oxygen atoms are located very close to the carbon backbone and the anhydride oxygen atoms far above it [i.e., 0.32 Å above the carbon backbone on Cu(100), and 0.23 Å on Cu(111)]. However, second, we note that while on Cu(111) the carboxylic oxygen atoms are located significantly above the carbon backbone [0.07 Å], on Cu(100) this difference [0.03 Å] is within the range of experimental uncertainty [0.05 Å]. Yet, at the same time it is noteworthy that the carboxylic oxygens on Cu(100) are not below the backbone, as is the case on all low index Ag surfaces. We thus find that the specific distortion motif present on Cu(111), i.e., the upwards shift of the carboxylic oxygen

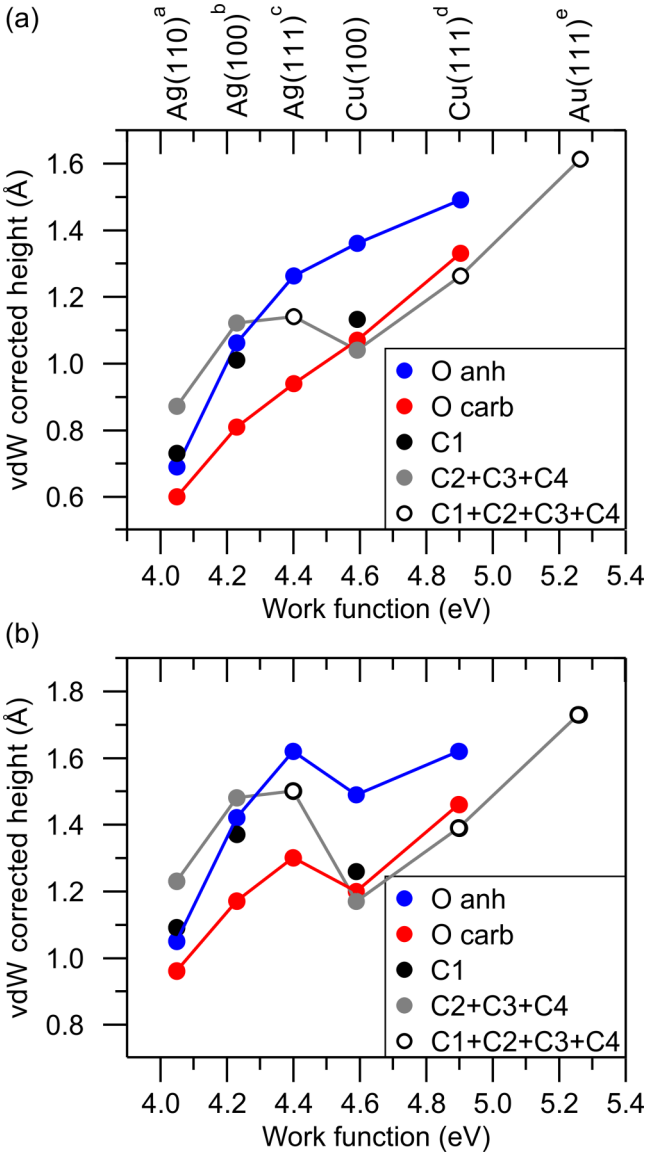

FIG. 12. Van der Waals-reduced adsorption heights [Eq. (1)] of PTCDA on noble metal surfaces, as determined by NIXSW (a [12], b [10], c [5], d [8], and e [4]), plotted as a function of the work function of the bare metal surface ($\Phi_{Ag(hkl)}$ [14], $\Phi_{Cu(100)}$ [18], $\Phi_{Cu(111)}$ [19], and $\Phi_{Au(111)}$ [39]). Experimentally [40] determined vdW radii are used in panel (a), theoretically [41] determined ones in (b). For Au(111), Ag(111), and Cu(111), the atoms from the carbon backbone (C2+C3+C4) and the functional carbon atoms (C1) were not analyzed differentially. For these cases, the average heights are marked with black open circles. The lines are guides to the eye.

atoms relative to the carbon backbone that is apparent when comparing Cu(111) to all three low index Ag surfaces, is also present on Cu(100), albeit to a reduced degree. This indicates that the bonding mechanism of PTCDA on the two investigated Cu surfaces are similar among themselves and at the same time different from those on the three Ag surfaces. Having said this, the position of the carboxylic oxygen atoms below the functional carbon (C1) on Cu(100) bears some resemblance with the situation on Ag surfaces.

The different overall distortions motifs of PTCDA on Cu and Ag surfaces indicate that the balance between the carbon-substrate and carboxylic oxygen-substrate interactions is a different one on Cu and Ag surfaces. However, it is not *a priori* clear whether the carboxylic oxygens on Cu are *less* interacting with the substrate than on Ag (and therefore relative to the carbon backbone further away from the surface), or whether the carbon backbone on Cu is *more* interacting with the substrate than on Ag (and therefore relative to the carboxylic oxygen atoms closer to the surface).

An answer to this puzzle comes by considering the second question raised in the introduction, namely the one regarding the validity of the (monotonous) scaling of vdW-corrected adsorption heights with work functions of the bare substrates also for the case of PTCDA adsorption on Cu(100). Indeed, in Fig. 12, we find that the trend of increasing adsorption heights with increasing work functions is fulfilled on the two Cu surfaces among themselves just as on the three low-index Ag surfaces among themselves. But most importantly, Fig. 12 also reveals that there is a discontinutiy in this trend when the surface changes from Ag to Cu. The strength of this discontinuity depends on which van der Waals radii are used for the substrate [panels (a) or (b)]. Specifically, if experimental van der Waals radii are used for the substrate [panel (a)], the discontinuity appears only for the carbon backbone, while for theoretical van der Waals radii [panel (b)] the discontinuity appears for all analyzed species.

Crucially, the stronger downward discontinuity of vdW-corrected adsorption heights for the carbon backbone as compared to the oxygen species indicates that on Cu the binding by the extended π system of the carbon backbone is becoming disproportionately stronger in comparison to the corresponding carboxylic oxygen-substrate interactions. In the light of the bonding mechanism of PTCDA on Ag surfaces, which we have interpreted in terms of local covalent O-Ag bonds and a (partially) repulsive interaction for the carbon backbone [10], this result suggests a crucial difference between Ag and Cu surfaces: on Cu the interaction between the carbon backbone and surface is clearly attractive. This may be the result of a surface binding potential for the carbon backbone whose minimum moves more strongly towards the surface than that of the oxygen species when going from Ag to Cu surfaces.

Nevertheless, it appears that the attractive Cu-C bonding is on Cu(100) still supported by covalent Cu-O bonds of the carboxylic oxygen atoms. There are several indications for this. Firstly, the vdW radius of oxygen is 1.50 Å [40]. This means that on Cu(100), where the vdW-corrected adsorption height of the carboxylic oxygen atoms is substantially below this value [$\approx$1.0 Å in Fig. 12(a) and $\approx$1.2 Å in Fig. 12(b)], an attractive interaction between the carboxylic oxygen atoms and the Cu surface appears very likely, similar to the situation on the three Ag surfaces. In fact, on Cu(100) the vdW-corrected adsorption height of the carboxylic oxygen atoms is very close to that of the carbon backbone, supporting the notion of an attractive interaction of the carboxylic oxygen atoms with the substrate.[1]

[1]This is to be contrasted with the situation of the anhydride oxygens, which on all surfaces except Ag(110) are found substantially above

An attractive interaction between the carboxylic oxygen atoms and the Cu(100) surfaces is, thirdly, supported by the adsorption site of PTCDA on Cu(100) (cf. Fig. 11). Specifically, the carboxylic oxygen atoms adsorb as close to on-top positions as the geometry of the substrate and the molecule allows, which is advantageous for forming local Cu-O bonds. In contrast, in the unfavored configuration A, these atoms would be located at bridge sites. In this context the comparison to other substrate surfaces is interesting as well. As on Cu(100), PTCDA adsorbs on Ag(111) [43], Ag(100) [10,11], and Ag(110) [44] with the carboxylic oxygen atoms close to on-top positions. It seems that local O-metal bonds are established in all cases, as is indeed suggested by their vdW-corrected adsorption heights, all of which are substantially below the van der Waals radius of oxygen (1.50 Å [40]).

However, a glance at Fig. 11 shows that not only the carboxylic oxygen atoms are found close to on-top positions. In the experimentally validated configuration B, several atoms of the carbon backbone are also adsorbed close to on-top positions of the substrate. Since this yields a better overlap between the π system and the Cu atoms of the surface (compared to the excluded configuration A), this observation supports the suggested attractive bond between the π system and the Cu surface. In fact, the lateral alignment of the carbon backbone, as well as of the carboxylic oxygen atoms, with on-top positions may explain why configuration B is preferred over A. Also the positions of the functional carbons (C1) fit into this picture. They are located at hollow sites, and therefore the interaction with the substrate is reduced, which in turn leads to their observed higher adsorption heights (+0.09 Å) compared to that of the carbon backbone.

We close the discussion of the adsorption height data in Fig. 12 by drawing attention to the following subtlety regarding the comparison between Cu(100) and Cu(111) surfaces. While on Cu(100) the carboxylic oxygen atoms are found below the functional carbon atoms (C1), on Cu(111) they are above the average position of all carbon atoms. A direct comparison of the precise distortion motifs on Cu(100) and Cu(111) is difficult, because the Cu(111) data do not distinguish between the carbon backbone and the functional carbons. However, experiments on $Cu_3Au(111)$, a surface that is very similar to Cu(111) [13], reveal that the carboxylic oxygen atoms are found above both the functional carbon (C1) and the carbon backbone. If this result can be regarded as representative also for the pure Cu(111) surface, it suggests a subtle difference between the situations on Cu(100) and on Cu(111), in spite of the similarity of the overall distortion motif on these two Cu surfaces that was mentioned above: In the case of the Cu(111) surface, the carboxylic oxygens do not seem to bind (in full accordance with a vdW-corrected adsorption height very close to the oxygen van der Waals radius of 1.50 Å [40]), while on the Cu(100) surface they do.

Finally, we note that a strong interaction of the carbon backbone with the Cu surface is also suggested by angle-resolved photoemission spectroscopy which reveals a strong intermolecular dispersion of the lowest unoccupied molecular orbital that becomes occupied through charge transfer upon adsorption [45].

both the functional carbon and the carboxylic oxygens which thus definitely do not bind (see Ref. [10]). On Cu(111), e.g., the vdW-corrected adsorption height of anhydride oxygen is close the oxygen van der Waals radius or even above.

V. CONCLUSION

Using the NIXSW technique, we determined the adsorption height and lateral adsorption site of PTCDA/Cu(100). In comparison with analogous structural data from other coinage metal surfaces, we conclude that Cu surfaces [data for Cu(100) and Cu(111) surfaces are available] exhibit the tendency to stabilize PTCDA closer to the surface than expected on the basis of extrapolated trends that have been established through an analysis of metallic van der Waals radii and work functions. Since the tendency to shorter adsorption heights is particularly effective for carbon atoms in PTCDA, it leads to different distortion motifs of PTCDA on Ag and Cu surfaces. We explain our observations by an attractive interaction between the carbon backbone of PTCDA and Cu surfaces. In the case of Cu(100), this Cu-C interaction is complemented by local bonds between carboxylic oxygen atoms and Cu atoms. Both the Cu-C and the Cu-O interactions lead to an adsorption site in which many carbon and oxygen atoms of PTCDA are adsorbed close to on-top positions.

ACKNOWLEDGMENTS

We thank C. Kumpf, G. van Straaten, and J. van Bebber for experimental support and M. Franke and F. C. Posseik for further development of Torricelli as well as for experimental support. We thank Diamond Light Source for access to beamline I09 (SI9722-1) and the team of I09, T.-L. Lee and P. Kumar. Financial support by the DFG under the project So407/6-1 is acknowledged. F.S.T. thanks A. Tkatchenko for helpful discussions.

APPENDIX A: NONDIPOLAR CORRECTION PARAMETERS

Taking into account that the sample is tilted by an angle ψ from the normal incidence geometry (cf. Fig. 2), the following formulas were used to calculate the nondipolar correction parameters in Eq. (2). The derivation and further details are given in Ref. [31]. The values for the angular distribution parameter γ and the scattering phase shifts δ_p, δ_d are given in Table IV.

$$S_R = P^2 \frac{1+Q_h}{1+Q_0}, \tag{A1}$$

$$S_I = |S_I| e^{i\Psi} = P \frac{1+\frac{Q_h+Q_0}{2}+i\tan\Delta\frac{Q_h-Q_0}{2}}{1+Q_0}. \tag{A2}$$

P, Q_h, Q_0, and Δ are defined by

$$P = \frac{\cos(\theta+2\psi)}{\cos(\theta)}, \tag{A3}$$

$$Q_h = \frac{\gamma}{3}\sin(\theta+2\psi), \tag{A4}$$

$$Q_0 = -\frac{\gamma}{3}\sin(\theta), \tag{A5}$$

$$\Delta = \delta_d - \delta_p. \tag{A6}$$

TABLE IV. Angular distribution parameter γ and scattering phase shifts δ_p, δ_d for the C 1s and O 1s photoemission for the (200) reflection with $E^{(200)}_{\text{Bragg}} = 3.4319$ keV and for the (111) reflection with $E^{(111)}_{\text{Bragg}} = 2.9721$ keV, as used in this work.

	γ	δ_p	δ_d
		(200) reflection	
C 1s	1.249	0.7397	0.5544
O 1s	1.174	0.9324	0.6764
		(111) reflection	
C 1s	1.144	0.7713	0.5724
O 1s	1.059	0.9738	0.6968

For strictly normal incidence ($\psi = 0$), $Q = Q_h = -Q_0$. This reduces the formulas for S_R and S_I to the well-known equations [27]. The calculated values for S_R, $|S_I|$, and Ψ are given in Table V as a function of the angle θ.

APPENDIX B: MEAN COHERENT POSITION AND FRACTION

Since the PE intensity varies by roughly a factor 2 between the different analyzer slices k, the corresponding error bars of P_c^k and F_c^k are also very different, see Fig. 5. It is clear that the P_c^k, F_c^k with larger error bars should contribute with smaller weights to the averages P_c, F_c over the different slices. The weights w_k were determined from the error bars $\sigma^k_{P_c}$ and $\sigma^k_{F_c}$ of the coherent positions and fractions that result from the quality of the PE yield fit.

TABLE V. Nondipolar correction parameters for C 1s and O 1s for the (200) and (111) reflections, as a function of the angle θ. Whenever the PE signal was integrated across the entire acceptance angle of the analyzer, the mean angle of 13.4° was used to calculate the nondipolar correction parameters.

	θ	S_R	$\lvert S_I\rvert$	Ψ
		(200) reflection		
C 1s	3.5°	1.071	1.036	-0.888×10^{-2}
	10.2°	1.145	1.075	-1.765×10^{-2}
	16.8°	1.220	1.116	-2.607×10^{-2}
	23.3°	1.292	1.156	-3.404×10^{-2}
	13.4°	1.181	1.096	-2.177×10^{-2}
O 1s	3.5°	1.065	1.033	-1.168×10^{-2}
	10.2°	1.133	1.069	-2.320×10^{-2}
	16.8°	1.200	1.105	-3.425×10^{-2}
	23.3°	1.263	1.142	-4.472×10^{-2}
	13.4°	1.165	1.086	-2.860×10^{-2}
		(111) reflection		
C 1s	−19.9°	0.862	0.934	2.161×10^{-2}
	−6.6°	0.970	0.985	0.446×10^{-2}
	+6.9°	1.095	1.049	-1.318×10^{-2}
	+20.0°	1.222	1.118	-2.964×10^{-2}
O 1s	−19.9°	0.876	0.941	2.825×10^{-2}
	−6.6°	0.973	0.986	0.583×10^{-2}
	+6.9°	1.085	1.043	-1.723×10^{-2}
	+20.0°	1.196	1.105	-3.874×10^{-2}

Technically, the weighted average was carried out in the following way. The real and imaginary parts of the Argand vector $\mathbf{P}_c^k = F_c^k\, e^{2\pi i P_c^k}$ were calculated from

$$\Re\left(\mathbf{P}_c^k\right) = F_c^k \cos\left(2\pi\, P_c^k\right),$$
$$\Im\left(\mathbf{P}_c^k\right) = F_c^k \sin\left(2\pi\, P_c^k\right). \tag{B1}$$

Their errors $\sigma^k_{\Re}$ and $\sigma^k_{\Im}$ were determined from $\sigma^k_{P_c}$ and $\sigma^k_{F_c}$ by standard error propagation. Next, the weighted averages of $\Re(\mathbf{P}_c^k)$ and $\Im(\mathbf{P}_c^k)$ were calculated, using the weights $w^k_{\Re} = (\sigma^k_{\Re})^{-2}$ and $w^k_{\Im} = (\sigma^k_{\Im})^{-2}$,

$$\overline{\Re(\mathbf{P}_c)} = \frac{1}{\sum_k w^k_{\Re}} \sum_k w^k_{\Re} \Re\left(\mathbf{P}_c^k\right),$$
$$\overline{\Im(\mathbf{P}_c)} = \frac{1}{\sum_k w^k_{\Im}} \sum_k w^k_{\Im} \Im\left(\mathbf{P}_c^k\right). \tag{B2}$$

The errors of the so-derived mean values were calculated from

$$\sigma_{\Re} = \sqrt{\frac{1}{n-1}\sum_k \left(\Re\left(\mathbf{P}_c^k\right) - \overline{\Re(\mathbf{P}_c)}\right)^2},$$
$$\sigma_{\Im} = \sqrt{\frac{1}{n-1}\sum_k \left(\Im\left(\mathbf{P}_c^k\right) - \overline{\Im(\mathbf{P}_c)}\right)^2}. \tag{B3}$$

Finally, the mean coherent position P_c and the mean coherent fraction F_c were calculated from $\overline{\Re(\mathbf{P}_c)}$ and $\overline{\Re(\mathbf{P}_c)}$ by inverting equations (B1) for the mean values. The corresponding uncertainties σ_{P_c} and σ_{F_c} are calculated from $\sigma_{\Re}$ and $\sigma_{\Im}$ by standard error propagation.

APPENDIX C: REDUCTION OF THE COHERENT FRACTION

Coherent fractions for the (200) reflection smaller than 1 indicate vertical disorder, i.e. disorder perpendicular to the (200) planes. This vertical disorder is described by the parameter $\delta_{(200)}$, as introduced in Fig. 8. As is evident from Eq. (7), the vertical disorder also reduces the coherent fraction for the (111) reflection. Here we will derive equation (7). For clarity, coherent fractions and positions that are not labeled refer to the (111) reflection.

The relation between the height distribution $f(z)$ and the coherent fraction F_c is given by following formula:

$$F_c e^{2\pi i P_c} = \int_0^{d_{hkl}} f(z) e^{2\pi i z/d_{hkl}} dz. \tag{C1}$$

We assume a Gaussian height distribution with mean value $P_c d_{hkl}$ and a standard deviation of δ:

$$f(z) = \frac{1}{\delta\sqrt{2\pi}} e^{-\frac{1}{2}(z - P_c d_{hkl})^2/\delta^2}. \tag{C2}$$

Inserting Eq. (C2) into Eq. (C1), performing the substitution

$$\xi = \frac{z - P_c d_{hkl}}{\sqrt{2}\delta}, \quad \frac{dz}{d\xi} = \sqrt{2}\delta, \tag{C3}$$

and using the assumption $\delta \ll d_{hkl}$ to extend the bounds of the integration leads to

$$F_c e^{2\pi i P_c} = \frac{1}{\sqrt{\pi}} e^{2\pi i P_c} \int_{-\infty}^{\infty} e^{-(\xi^2 - i\sqrt{8}\pi\delta\xi/d_{hkl})} d\xi. \tag{C4}$$

This yields

$$F_c = \frac{1}{\sqrt{\pi}} \int_{-\infty}^{\infty} \left(e^{-\xi^2} \cos \frac{\sqrt{8}\pi\delta\xi}{d_{hkl}} + i e^{-\xi^2} \sin \frac{\sqrt{8}\pi\delta\xi}{d_{hkl}} \right) d\xi. \tag{C5}$$

Since the second summand is an uneven function, its integral will vanish. Using [46]

$$\int_0^{\infty} e^{-a^2x^2} \cos bx \, dx = \frac{\sqrt{\pi}}{2a} e^{-b^2/4a^2}, \tag{C6}$$

and the fact that the first summand is an even function, the expression for the coherent fraction becomes

$$F_c = e^{-2(\pi\delta)^2/d_{hkl}^2}. \tag{C7}$$

A similar formula is used to take into account thermal vibrations [24].

Now we can calculate the standard deviation δ^i_{200} of the height distribution $f(z)^i$ from the experimentally determined $F^i_c(200)$:

$$\delta^i_{200} = \frac{d_{200}}{\pi} \sqrt{-\frac{1}{2} \ln F^i_c(200)}. \tag{C8}$$

δ^i_{111} and δ^i_{200} are simply connected by a trigonometric function (cf. inset of Fig. 8):

$$\delta^i_{111} = \delta^i_{200} \cos\alpha. \tag{C9}$$

Since $\cos\alpha = 1/\sqrt{3}$ and $d_{200} = \sqrt{3}/2\, d_{111}$, it follows that

$$\delta^i_{(111)} = \frac{1}{2} \frac{d_{111}}{d_{200}} \delta^i_{(200)}. \tag{C10}$$

Using Eq. (C7), we thus obtain

$$F^i_c = F^i_{c,0} \sqrt[4]{F^i_c(200)}. \tag{C11}$$

This last equation assumes a multiplication of the coherent fractions due to disorder and structural effects.

[1] A. Tkatchenko, L. Romaner, O. T. Hofmann, E. Zojer, C. Ambrosch-Draxl, and M. Scheffler, MRS Bull. **35**, 435 (2011).
[2] L. Kronik and A. Tkatchenko, Acc. Chem. Res. **47**, 3208 (2014).
[3] F. S. Tautz, Prog. Surf. Sci. **82**, 479 (2007).
[4] S. Henze, O. Bauer, T.-L. Lee, M. Sokolowski, and F. S. Tautz, Surf. Sci. **601**, 1566 (2007).
[5] A. Hauschild, K. Karki, B. C. C. Cowie, M. Rohlfing, F. S. Tautz, and M. Sokolowski, Phys. Rev. Lett. **94**, 036106 (2005).
[6] R. Rurali, N. Lorente, and P. Ordejón, Phys. Rev. Lett. **95**, 209601 (2005).
[7] A. Hauschild, K. Karki, B. C. C. Cowie, M. Rohlfing, F. S. Tautz, and M. Sokolowski, Phys. Rev. Lett. **95**, 209602 (2005).
[8] A. Gerlach, S. Sellner, F. Schreiber, N. Koch, and J. Zegenhagen, Phys. Rev. B **75**, 045401 (2007).
[9] A. Hauschild, R. Temirov, S. Soubatch, O. Bauer, A. Schöll, B. C. C. Cowie, T.-L. Lee, F. S. Tautz, and M. Sokolowski, Phys. Rev. B **81**, 125432 (2010).
[10] O. Bauer, G. Mercurio, M. Willenbockel, W. Reckien, C. Heinrich Schmitz, B. Fiedler, S. Soubatch, T. Bredow, F. S. Tautz, and M. Sokolowski, Phys. Rev. B **86**, 235431 (2012).
[11] M. Willenbockel, *Interacting Interactions: A Study on the Interplay of Molecule-Molecule and Molecule-Substrate Interactions at Metal-Organic Interfaces*, Schriften des Forschungszentrums Jülich, Reihe Schlüsseltechnologien/Key Technologies, Vol. 99 (2014).
[12] G. Mercurio, O. Bauer, M. Willenbockel, N. Fairley, W. Reckien, C. H. Schmitz, B. Fiedler, S. Soubatch, T. Bredow, M. Sokolowski, and F. S. Tautz, Phys. Rev. B **87**, 045421 (2013).
[13] O. Bauer, Ph.D. thesis, University of Bonn (2015), available at http://hss.ulb.uni-bonn.de/2015/4233/4233.html.
[14] M. Willenbockel, D. Lüftner, B. Stadtmüller, G. Koller, C. Kumpf, S. Soubatch, P. Puschnig, M. G. Ramsey, and F. S. Tautz, Phys. Chem. Chem. Phys. **17**, 1530 (2015).
[15] M. Rohlfing, R. Temirov, and F. S. Tautz, Phys. Rev. B **76**, 115421 (2007).
[16] V. G. Ruiz, W. Liu, E. Zojer, M. Scheffler, and A. Tkatchenko, Phys. Rev. Lett. **108**, 146103 (2012).
[17] S. Gärtner, B. Fiedler, O. Bauer, A. Marele, and M. M. Sokolowski, Beilstein J. Org. Chem. **10**, 2055 (2014).
[18] X. F. Wang, W. Li, J. G. Lin, and Y. Xiao, Europhys. Lett. **89**, 66004 (2010).
[19] S. Duhm, A. Gerlach, I. Salzmann, B. Bröker, R. Johnson, F. Schreiber, and N. Koch, Org. Electron. **9**, 111 (2008).
[20] A. Schmidt, T. J. Schuerlein, G. E. Collins, and N. R. Armstrong, J. Phys. Chem. **99**, 11770 (1995).
[21] M. Andreasson, M. Tengelin-Nilsson, L. Ilver, and J. Kanski, Synth. Met. **158**, 45 (2008).
[22] L. Kilian, W. Weigand, E. Umbach, A. Langner, M. Sokolowski, H. L. Meyerheim, H. Maltor, B. C. C. Cowie, T. Lee, and P. Bäuerle, Phys. Rev. B **66**, 075412 (2002).
[23] A. Schöll, Y. Zou, M. Jung, T. Schmidt, R. Fink, and E. Umbach, J. Chem. Phys. **121**, 10260 (2004).
[24] J. Zegenhagen, Surf. Sci. Rep. **18**, 202 (1993).
[25] D. P. Woodruff, Prog. Surf. Sci. **57**, 1 (1998).
[26] D. P. Woodruff, Rep. Prog. Phys. **68**, 743 (2005).
[27] J. Zegenhagen and A. Kazimirov, *The X-ray Standing Wave Technique: Principles and Applications*, World Scientific Series on Synchrotron Radiation Techniques and Applications (World Scientific, Singapore, 2012).
[28] G. Mercurio, *Study of Molecule-Metal Interfaces by Means of the Normal Incidence X-ray Standing Wave Technique*, Schriften des Forschungszentrums Jülich, Reihe Schlüsseltechnologien/Key Technologies, Vol. 49 (2012).
[29] C. J. Fisher, R. Ithin, R. G. Jones, G. J. Jackson, D. P. Woodruff, and B. C. C. Cowie, J. Phys.: Condens. Matter **10**, L623 (1998).
[30] I. A. Vartanyants and J. Zegenhagen, Solid State Commun. **113**, 299 (2000).

[31] G. van Straaten, M. Franke, F. C. Bocquet, F. S. Tautz, and C. Kumpf, J. Electron Spectros. Related Phenom. (2017).
[32] M. B. Trzhaskovskaya, V. I. Nefedov, and V. G. Yarzhemsky, At. Data Nucl. Data Tables **77**, 97 (2001).
[33] A. Jablonski, F. Salvat, and C. J. Powell, *NIST Electron Elastic-Scattering Cross-Section Database—Version 3.2* (National Institute of Standards and Technology, Gaithersburg, MD, 2010).
[34] TORRICELLI is an XSW data analysis and simulation program written by G. Mercurio, M. Franke, and F. C. Bocquet. Copies can be obtained from s.tautz@fz-juelich.de.
[35] D. Woodruff, Nucl. Instrum. Methods Phys. Res., Sect. A **547**, 187 (2005).
[36] N. J. Simon, E. S. Drexler, and R. P. Reed, *Properties of copper and copper alloys at cryogenic temperatures*, NIST Monograph Vol. 177 (Gaithersburg, MD : NIST, 1992).
[37] B. Batterman and C. Henderson, Rev. Mod. Phys. **36**, 681 (1964).
[38] M. J. Frisch, G. W. Trucks, H. B. Schlegel, G. E. Scuseria, M. A. Robb, J. R. Cheeseman, J. A. Montgomery, Jr., T. Vreven, K. N. Kudin, J. C. Burant, J. M. Millam, S. S. Iyengar, J. Tomasi, V. Barone, B. Mennucci, M. Cossi, G. Scalmani, N. Rega, G. A. Petersson, H. Nakatsuji, M. Hada, M. Ehara, K. Toyota, R. Fukuda, J. Hasegawa, M. Ishida, T. Nakajima, Y. Honda, O. Kitao, H. Nakai, M. Klene, X. Li, J. E. Knox, H. P. Hratchian, J. B. Cross, V. Bakken, C. Adamo, J. Jaramillo, R. Gomperts, R. E. Stratmann, O. Yazyev, A. J. Austin, R. Cammi, C. Pomelli, J. W. Ochterski, P. Y. Ayala, K. Morokuma, G. A. Voth, P. Salvador, J. J. Dannenberg, V. G. Zakrzewski, S. Dapprich, A. D. Daniels, M. C. Strain, O. Farkas, D. K. Malick, A. D. Rabuck, K. Raghavachari, J. B. Foresman, J. V. Ortiz, Q. Cui, A. G. Baboul, S. Clifford, J. Cioslowski, B. B. Stefanov, G. Liu, A. Liashenko, P. Piskorz, I. Komaromi, R. L. Martin, D. J. Fox, T. Keith, M. A. Al-Laham, C. Y. Peng, A. Nanayakkara, M. Challacombe, P. M. W. Gill, B. Johnson, W. Chen, M. W. Wong, C. Gonzalez, and J. A. Pople, *Gaussian* (Gaussian, Inc., Wallingford, CT, 2004).
[39] G. V. Hansson and S. A. Flodström, Phys. Rev. B **18**, 1572 (1978).
[40] A. Bondi, J. Phys. Chem. **68**, 441 (1964).
[41] V. G. Ruiz, W. Liu, and A. Tkatchenko, Phys. Rev. B **93**, 035118 (2016).
[42] H. L. Davis and J. R. Noonan, J. Vac. Sci. Technol. **20**, 842 (1982).
[43] A. Kraft, R. Temirov, S. K. M. Henze, S. Soubatch, M. Rohlfing, and F. S. Tautz, Phys. Rev. B **74**, 041402(R) (2006).
[44] M. Böhringer, W.-D. Schneider, K. Glöckler, E. Umbach, and R. Berndt, Surf. Sci. **419**, L95 (1998).
[45] D. Lüftner, S. Weiß, P. Hurdax, X. Yang, V. Feyer, A. Gottwald, G. Koller, S. Soubatch, P. Puschnig, M. G. Ramsey, and F. S. Tautz (unpublished).
[46] I. Bronstein, K. Semedjajew, G. Musiol, and H. Mühlig, *Taschenbuch der Mathematik*, 6th ed. (Verlag Harri Deutsch GmbH, Frankfurt am Main, 2006).